Transportation Geotechnics 54 (2025) 101628

Contents lists available at ScienceDirect

Transportation Geotechnics

journal homepage: www.elsevier.com/locate/trgeo

Original article

A level-set method-based framework for modeling abrasion of railway ballast

Haoran Jiang [a], Opu Chandra Debanath [b,*], Yang Li [c], Ruidong Li [d]

[a] Civil Engineering Design Division, Kajima Corporation, 3-8, Motoakasaka, 1-chome, Minato-ku, Tokyo, 107-8477, Japan
[b] Department of Civil Engineering, Chittagong University of Engineering and Technology, Chattogram 4349, Bangladesh
[c] Department of Civil Engineering, Kyushu University, Fukuoka 819-0395, Japan
[d] Department of Civil and Environmental Engineering, The Hong Kong Polytechnic University, Hung Hom, Kowloon, Hong Kong, China

ARTICLE INFO

Keywords:
Gaussian curvature-driven abrasion model
Railway ballast
Realistic shape modeling
LS-DEM
Triaxial compression

ABSTRACT

Particle abrasion is a critical phenomenon in the study of granular materials, as it leads to a progressive decrease in the mechanical strength of the granular aggregates. In this study, we present a novel computational framework based on Firey's law for predicting the abrasion-induced shape evolution of railway ballast. This approach provides a more efficient alternative to laboratory experiments for generating abraded particle shapes for use in numerical simulations. Using 3D scans of fresh ballast particles, we simulate their abrasion process at various levels of mass loss and statistically analyze the resulting shape changes. We then adopt the level-set discrete element method (LS-DEM) to investigate their mechanical response under triaxial compression. Macroscopically, both the stress ratio and void ratio decrease with increasing abrasion level, which can be attributed to abrasion-induced corner rounding and surface smoothing. Microscopically, the decrease in stress ratio is associated with the loss of highly stable contact subnetworks characterized by larger contact deviation angles, and the weakening of contact network anisotropy. Meanwhile, the decrease in void ratio is attributable to the transition of ballast particles toward more ellipsoid-like shapes, which promotes denser packings.

1. Introduction

The study of degradation of granular materials is, among many other applications, important in railway ballast [1–6]. As ballast rocks degrade, the strength and compactness of the ballast layer are altered, which can lead to significant issues such as differential ballast settlement [7], reduced lateral resistance [8], and restricted drainage capacity [9]. Thus, predicting the degradation of ballast rocks and understanding its impact on the behavior of railway ballast are crucial. Generally, crushing and abrasion are two primary degradation modes that occur in railway ballast subjected to train loading: crushing is a sudden process that typically occurs under higher loads and produces many small, angular fragments [10], whereas abrasion is a gradual process that occurs under lower loads and tends to blunt the edges and corners of particles [3]. While crushing is certainly an important process that greatly affects mechanical behavior, the research herein focuses on the abrasion aspect.

Past research on the abrasion of granular materials has focused on quantitative evaluations through experimental investigations [11–13] and theoretical abrasion models [14–16]. Experimentally, researchers primarily use the Los Angeles Abrasion (LAA) and micro-Deval tests to assess the abrasion resistance of various ballast materials under different conditions. Deiros Quintanilla et al. [17] conducted a standard micro-Deval test on granite ballast and analyzed the resulting changes in particle morphology via X-ray computed tomography. They found that up to 5% abrasion, the overall form of ballast particles remained largely unchanged, while asperity features showed significant differences. Similarly, Ge et al. [18] observed that limestone aggregate worn by the LAA tester undergoes shape changes mainly in the early stages of abrasion, with highly angular particles rapidly degrading to attain higher sphericity. Other experimental studies have focused on the comparison of different materials. For example, Paixão and Fortunato [19] examined the abrasion resistance of granite rock and steel furnace slag, finding that the latter has lower abrasion resistance than granite rock. Despite differences in purpose or testing methodology, these experimental studies all indicate that particles become less angular and smoother as they abrade. This suggests that there must be a relationship between the local curvature of particles and the amount of local abrasion.

From a theoretical perspective, Firey's law [14] successfully relates abrasion depth to local curvature. Specifically, they derived a geometric partial differential equation to model shape evolution of a convex particle under repeated collisions, stating that abrasion occurs

* Corresponding author.
E-mail address: debnathopu@cuet.ac.bd (O.C. Debanath).

https://doi.org/10.1016/j.trgeo.2025.101628
Received 3 February 2025; Received in revised form 31 May 2025; Accepted 23 June 2025
Available online 7 July 2025

normal to the surface at a rate proportional to the Gaussian curvature. Although Bloore [20] later extended this model by incorporating the effect of mean curvature to account for more general scenarios, the simple Firey's law has been proven sufficiently effective in closely replicating the actual abrasion process of limestone particle [16]. Other abrasion models, however, do not explicitly consider curvature and instead relate abrasion to other physical quantities [21,22]. For example, Archard's law states that the material volume abraded is linearly proportional to the amount of frictional work done. While this model has traditionally been applied to the wear of metal machine parts [22], it has recently been applied to the abrasion of geological materials [23, 24].

In terms of numerical efforts, the discrete element method (DEM) is increasingly popular for handling particulate systems, although the direct modeling of abrasive particles in DEM is still challenging. Unlike particle breakage, which occurs as a sudden event that can be captured by specific crushing criteria [25], particle abrasion is a continuous process, with the particle's surface being continually pulled inward, causing the shape to change over time. Therefore, incorporating abrasion into DEM simulations requires continuously updating particle shapes according to a predefined rule, which is inherently time-consuming. To date, the existing numerical studies evaluating the abrasion effects on railway ballast still rely on a combination of above-mentioned abrasion experiments and DEM simulations, with abraded particle shapes typically obtained from laboratory abrasion tests. For instance, Zhang et al. [26] conducted LAA drum tests on ballast specimens up to 2000 cycles and collected shape data from 100 particles using image analysis. These shapes were then reconstructed as 2D clumps for biaxial shearing, enabling a DEM investigation of the effects of abrasion-induced rounding on ballast's mechanical behavior. More recently, Binaree et al. [27] experimentally abraded fresh railway ballast up to a fouling index of 40% through an extended LAA test and further performed DEM biaxial tests to assess the impact of abrasion on both macro- and micro-mechanical properties. However, for simplicity, the fresh and deteriorated particles were respectively represented by elongated, angular polygons and rounded polygons. The simplified shape representations adopted in these studies were chosen primarily to avoid high computational costs. Tolomeo and McDowell [28] simulated realistic 3D ballast shapes using two different strategies, i.e., sphere-clumping and polyhedron methods, but were limited to modeling only 747 particles in the triaxial test due to the large number of sub-spheres or faces required to represent each particle. For more efficient ballast modeling, the level-set discrete element method (LS-DEM) is a potential alternative. As a well-established DEM approach with advanced contact detection technique, it has been shown to accurately capture realistic particle shapes and faithfully replicate experimental results [29]. Compared to the aforementioned shape representation approaches, LS-DEM provides greater computational efficiency in modeling irregular shapes, with the represented particles having smoothly varying curvature. Furthermore, the level-set framework facilitates the application of well-known curvature-based diffusion methods to abrade particles [30], significantly reducing the time and resources typically required for conventional abrasion experiments.

To overcome the limitations highlighted in existing DEM studies, where acquiring abraded ballast shapes often relies on time-consuming and resource-intensive experiments, this study presents a Gaussian curvature-driven model based on Firey's law to computationally abrade the railway ballast particles, enabling the generation of particle shapes at any desired abrasion level using only their initial geometries. This simple yet effective model enables the tracking of individual particle shape evolution, which is extremely difficult to achieve in physical experiments. We first quantitatively examine the evolution of particle shapes across scales by analyzing changes in shape parameters and surface asperities. We then adopt the LS-DEM approach to carry out a series of triaxial compression tests. Through a detailed analysis of macroscopic and contact-scale features, this study provides insights into the effects of particle abrasion on mechanical responses of quasi-statically loaded ballast specimens.

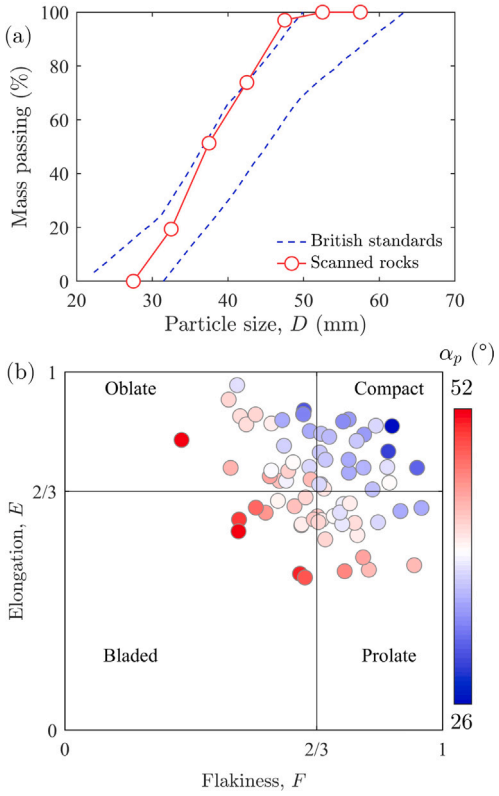

Fig. 1. (a) Particle size distribution for the 75 ballast scans (solid line) together with limits defined by the British standards (dashed lines) [28]. (b) Zingg's diagram for flakiness (F) and elongation (E) of 75 ballast particles using the ellipsoid fitting method. The color intensity indicates the corresponding α_p value.

2. Shape reconstruction of railway ballast

2.1. Scans of fresh railway ballast

This study uses the ballast scans provided by Li et al. [31], who employed a recently developed close-range photogrammetry technique to capture high-resolution images and reconstruct triangular meshes of fresh railway ballast. Detailed procedures for 3D scan acquisition and image data analysis are outlined in Paixão et al. [32]. From the available dataset, 75 representative ballast scans are carefully selected for analysis, ensuring that the particle size distribution (PSD) of the chosen particles, ranging between 20 mm and 60 mm, meets the standards of field samples (see Fig. 1(a)). It is important to note that the particle sizes are determined based on their volume-equivalent spheres, which may differ slightly from experimental measurements obtained through sieving process. Alternative approaches for PSD measurement that do not rely on physical sieving also exist, and a detailed comparison of these methods is discussed in Kumara et al. [33].

For the shape characterization, we first quantify the overall form of each 3D ballast particle using two form indices: flakiness (F) and elongation (E). A commonly used method to determine these indices is fitting an oriented bounding box (OBB) to the particle and then calculating F and E based on the ratios of the short-to-intermediate and intermediate-to-long dimensions of the bounding box, respectively. However, the OBB method is sensitive to the choice of the bounding box, which can lead to non-unique results. Alternatively, we employ a more robust approach by fitting an ellipsoid to the particle, where the ellipsoid is computed such that its three principal moments of inertia are identical to those of the original particle. The ellipsoid fitting method enables the unique derivation of flakiness ($F = S/I$) and elongation ($E = I/L$), where S, I, and L are the shortest,

intermediate, and longest axes of the fitted ellipsoid, respectively. By definition, both F and E range from 0 to 1, with values approaching 1 indicating a shape closer to a sphere. These shape metrics are plotted on a shape diagram shown in Fig. 1(b), referred to as Zingg's diagram. The shape distribution of fresh ballast particles shows large variability, although blade-like shapes (i.e., highly elongated and flattened shapes) are relatively rare. This is because such shapes have poor performance in resisting breakage, making them relatively less prevalent in railway ballast.

While form indices provide a general description of particle shape, they fail to capture finer morphological details such as local angularity and surface asperity. Angularity, in particular, is critical in the context of railway ballast due to its direct contribution to the strength and load-bearing capacity. However, angularity is highly susceptible to abrasion, which gradually rounds the sharp edges and corners. Therefore, a more comprehensive shape quantification is necessary to account for these finer-scale features. To achieve this, we adopt a mechanics-based shape index, α_p, also referred to as the rotational resistance angle. It is defined as:

$$\alpha_p = \frac{1}{A}\int_{\partial\Omega} \alpha \mathrm{dS}, \tag{1}$$

where A is the surface area of the particle, and α is the angle between the surface normal and the surface-to-centroid vector at a given point on the surface ($\partial\Omega$). Mechanically, a higher α_p gives the particle more rolling resistance, as normal forces acting on the particle tend to lock the particle in place. This parameter is positively correlated with angularity and surface asperity of particles [34,35], and has been recently employed in studies on railway ballast [28]. In this study, α_p value associated with each scanned ballast shape is represented by the color intensity of symbols in the shape diagram (Fig. 1(b)). It is observed that smaller values of E or F correspond to higher α_p values, suggesting that this indicator effectively incorporates large-scale shape features as well.

2.2. Level-set function for shape representation

The level-set function is a widely used mathematical tool for indicating the interface of a particle's shape. In this study, it is adopted for virtual shape representation due to its suitability for facilitating abrasion implementation and numerical modeling of railway ballast, as will be discussed in the following sections. A widely used level-set function is the signed distance function (SDF), $\phi(\mathbf{x})$, which measures the minimum Euclidean distance between a point ($\mathbf{x}$) and the particle boundary ($\partial\Omega$). It is defined as:

$$\phi(\mathbf{x}) = \pm \min(\|\mathbf{x}-\mathbf{y}\|), \quad \forall \mathbf{y} \in \partial\Omega, \tag{2}$$

where the sign of $\phi(\mathbf{x})$ is determined by the position of $\mathbf{x}$ relative to $\partial\Omega$: positive outside the particle and negative inside. While the level-set function is applicable to arbitrary shapes for shape reconstruction, explicit formulations exist only for a limited number of regular geometries, e.g., spheres and ellipsoids. To describe more general shapes such as railway ballast investigated here, a discretized level-set grid with uniform spacing is constructed, with the discrete signed distance values stored at its grid points. Within the grid boundaries, the signed distance value at any arbitrary point can be determined through trilinear interpolation of the values stored at neighboring grid points. Previous studies have demonstrated the reliability of this grid-based level-set approach for accurately capturing complex particle geometries [29,35,36]. An example is shown in Fig. 2, where a two-dimensional level-set grid effectively captures the boundary of a two-dimensional slice of the 3D particle.

In addition to shape representation, the level-set function enables the calculation of inertial properties of ballast particles, including mass, moment of inertia, and center of mass. This is crucial for modeling virtually present abraded particles generated by the computational model. The detailed calculation procedures are presented in Appendix.

3. A computational model for railway ballast abrasion

3.1. Implementation of a Gaussian curvature-driven abrasion model

The computational abrasion of fresh railway ballast is performed on their level-set functions using Gaussian curvature-driven flow [30]. As ϕ represents the level-set function, ϕ_t is thus the time derivative of ϕ, which can also be seen as the rate ($\mathrm{d}h/\mathrm{d}t$) at which the surface of the particle moves inward along the direction of inward normal. Here, h is the cumulative abrasion depth. According to Firey's law, there is a linear relationship between ϕ_t and the Gaussian curvature (K):

$$\phi_t = \mathrm{d}h/\mathrm{d}t = bK, \tag{3}$$

where b is a constant that controls the rate of shape evolution. For real-time abrasion prediction, b must be specified to reflect factors such as material hardness and loading conditions, where softer materials and more dynamic loading generally correspond to larger values of b. In this study, however, since we are only concerned with the shape of the particle as it abrades to specified levels of mass loss, b is arbitrary and is selected to ensure numerical stability. Furthermore, a sensitivity analysis is conducted to ensure that the chosen value of b falls within a moderate range, such that increasing it by an order of magnitude does not affect the resulting particle shape at a given mass-loss level.

Let ϕ_m be the mth spatial first derivative and ϕ_{mn} be the mnth spatial second derivative of ϕ. These spatial derivatives are computed using second-order accurate central difference schemes on the discrete level-set grid, and time stepping is performed using an explicit forward Euler scheme. Numerical stability is ensured by enforcing a stringent Courant–Friedrichs–Lewy (CFL) condition on the time step [30]. The Gaussian curvature, $K = \kappa_1\kappa_2$, with two exceptions, is computed from the level-set function as

$$K = \frac{\begin{array}{l}\phi_x^2(\phi_{yy}\phi_{zz}-\phi_{yz}^2)+\phi_y^2(\phi_{xx}\phi_{zz}-\phi_{xz}^2)+\phi_z^2(\phi_{xx}\phi_{yy}-\phi_{xy}^2)+\\ 2\left[\phi_x\phi_y(\phi_{xz}\phi_{yz}-\phi_{xy}\phi_{zz})+\phi_x\phi_z(\phi_{xy}\phi_{yz}-\phi_{xz}\phi_{yy})+\phi_y\phi_z(\phi_{xy}\phi_{xz}-\phi_{yz}\phi_{xx})\right]\end{array}}{\left(\phi_x^2+\phi_y^2+\phi_z^2\right)^2} \tag{4}$$

where κ_1 and κ_2 denote two principal curvatures. The exceptions arise from the assumption that abrasion only occurs at a convex point ($\kappa_1 > 0$ and $\kappa_2 > 0$) and that non-convex regions of the particle surface are not abraded (i.e., $\phi_t = 0$). This simplification is supported by experimental observations [17] and has also been adopted in theoretical models of collision-based abrasion [37]. Based on this assumption, the first exception is that K needs to be 0 where $K < 0$, as these are saddle regions on the particle where one principal curvature is positive and another is negative. The second exception is that K also needs to be set to 0 in regions where both principal curvatures are negative, but K does not indicate where these regions are as K is positive in these regions. Thus, the mean curvature (H), which is the average of the principal curvatures, $(\kappa_1+\kappa_2)/2$, also must be computed:

$$H = \frac{\phi_x^2(\phi_{yy}+\phi_{zz})+\phi_y^2(\phi_{xx}+\phi_{zz})+\phi_z^2(\phi_{xx}+\phi_{yy})-2(\phi_x\phi_y\phi_{xy}+\phi_x\phi_z\phi_{xz}+\phi_y\phi_z\phi_{yz})}{(\phi_x^2+\phi_y^2+\phi_z^2)^{3/2}}. \tag{5}$$

In regions where H is negative, at least one principal curvature is negative, and K is set to 0. Thus, K is computed as:

$$K = \begin{cases} 0 & \text{if } K<0 \text{ or } H<0, \\ \kappa_1\kappa_2 & \text{otherwise.} \end{cases} \tag{6}$$

We then implement the computational abrasion model for railway ballast as follows. The initial shapes of fresh railway ballast, represented by their level-set functions (ϕ), serve as the input for the analysis. As ϕ is discretized on a uniform grid, we adopt a fixed grid resolution of $D/d_{\mathrm{grid}} = 50$ to accurately capture the particle geometry

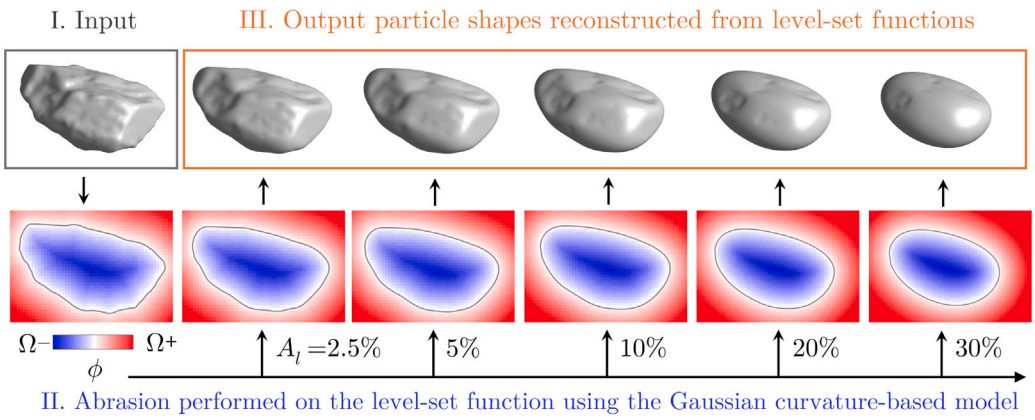

Fig. 2. Implementation of computational abrasion on railway ballast using a Gaussian curvature-driven model.

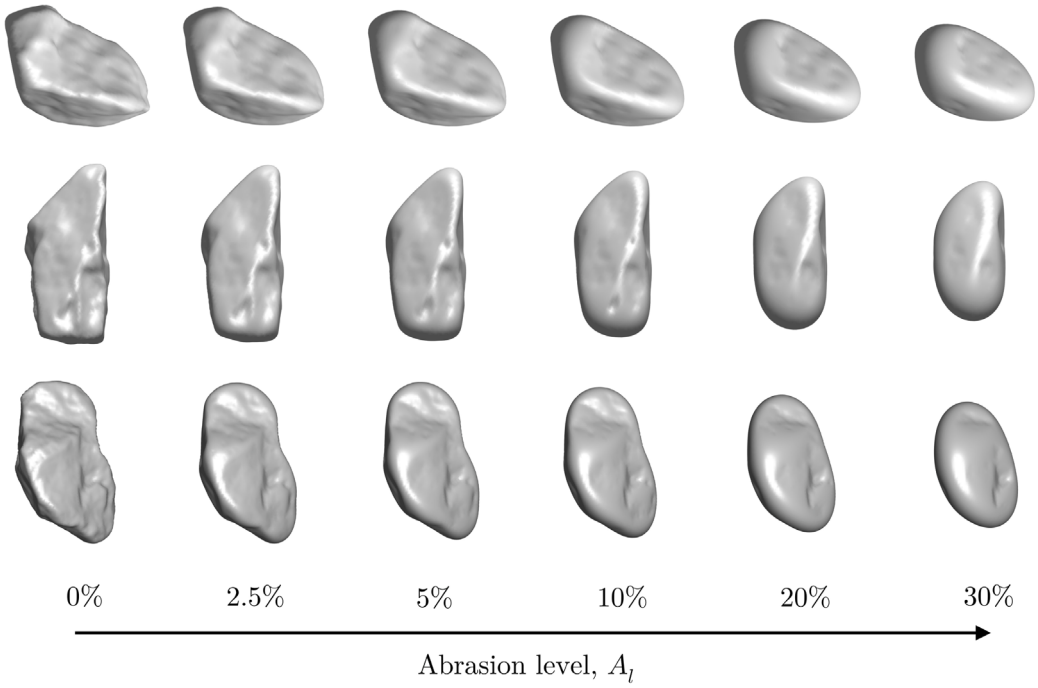

Fig. 3. Shape evolution of ballast particles at various abrasion levels.

and surface details [35], where d_{grid} denotes the grid spacing. The Gaussian curvatures (K) are evaluated using Eqs. (4)–(6), and the abrasion depth (dh) at each surface point is determined by Eq. (3). The abrasion process is conducted by moving the particle interface inward through modifying ϕ based on ϕ_t over a time increment (dt). At each subsequent dt step, the Gaussian curvature is recalculated based on the updated particle shape (i.e., the modified level-set function). This procedure is iteratively repeated to simulate progressive abrasion. Fig. 2 illustrates the main concept of the proposed computational abrasion model. In this study, all particles are slowly abraded and the shapes are recorded at six specified abrasion levels, defined by the percentage of mass loss $A_l \in \{0\%, 2.5\%, 5\%, 10\%, 20\%, 30\%\}$. Here, $A_l = 0\%$ corresponds to the initial, unabraded state, while $A_l = 30\%$ corresponds to a highly abraded condition that would require several hundred thousand cycles in a standard micro-Deval test to achieve in practice [17,38]. The selection of 30% as the upper limit is motivated by its practical significance, as this level of degradation is often regarded as the maintenance threshold for field ballast in many countries [39]. More examples of ballast abrasions are presented in Fig. 3, which shows how sharp edges and small-scale asperities gradually disappear due to abrasion. This results in a significant reduction in particle angularity and an overall smoother surface. However, despite these morphological changes, the general shape of the particles appears to remain largely unchanged.

3.2. Morphological evolution during abrasion

To more quantitatively capture the morphological changes during abrasion, Fig. 4 presents the variations in shape distributions of all 75 particles with respect to the abrasion level (A_l). Figs. 4(a–b) show that the cumulative distributions of E and F display only little change even when ballast particles are abraded up to 30%. This supports the visual observations in Fig. 3 that the overall form of the particles is largely preserved without remarkable changes. More importantly, it is consistent with the experimental findings of Domokos et al. [16], who noted that cuboids composed of oolitic limestone subjected to up to 45% abrasion in a rotating LAA drum retained their overall shape, with degradation occurring primarily at the edges. This also supports our view that form indices, such as E and F, are not comprehensive enough to capture abrasion-induced shape changes.

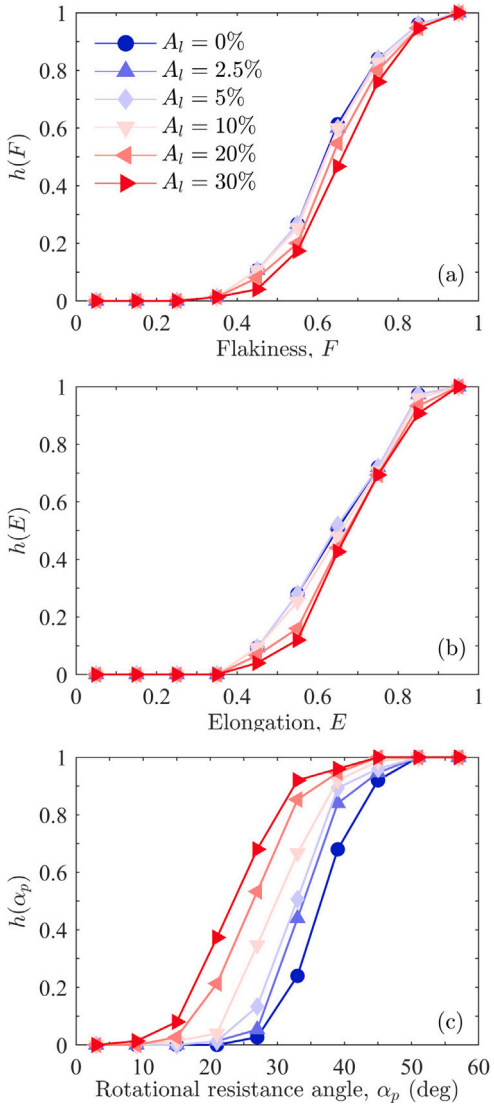

Fig. 4. Cumulative distributions of the shape indices (a) F, (b) E, and (c) α_p for ballast particles at various abrasion levels.

Fig. 4(c) further presents the cumulative distributions of α_p to track its variation during the abrasion process. The curves of $h(\alpha_p)$ exhibit a clear leftward shift with increasing A_l, corresponding to the decreasing shape irregularity. Since Jiang et al. [35] reported that the difference in α_p between a highly roughened ellipsoid and its smooth counterpart was less than 5 degrees, we can conclude that the observed variation in α_p here is primarily attributed to reductions in the angularity of ballast particles. Consequently, the gradual shift in $h(\alpha_p)$ suggests that the local angularity is reduced continuously throughout abrasion.

To accommodate the evolution of microscale morphological features, we track changes in local asperity radius (r_a) of ballast particles throughout the abrasion process. Following approaches proposed in previous experimental studies [17,19], we calculate r_a as follows. The curvature of surface points on the meshes is calculated using PyMeshLab [40] with the APSS algorithm [41]. As suggested, a spatial low-pass filter with a scale of 10 is applied. This parameter controls the range of the surrounding region considered when estimating curvature. A value of 10 has been recommended as a compromise between capturing fine asperity details and incorporating the neighboring surface area typically involved in ballast contacts [17,19]. Finally, r_a is computed as the reciprocal of the curvature, where a larger r_a value indicates a smoother surface. Fig. 5(a) illustrates the changes in surface asperity, characterized by $1/r_a$, for two individual particles as A_l increases. Lower magnitude of $1/r_a$ or lower color intensity corresponds to a smoother surface. Additionally, the positive or negative sign indicates the convex or concave surface, respectively. Our results for computationally abraded particles show that, sharp asperities rapidly disappear in the beginning, followed by slower surface smoothing effect with abrasion later on. This trend agrees well with the experimental observations by both Deiros Quintanilla et al. [17] and Paixão and Fortunato [19]. In particular, Deiros Quintanilla et al. [17] identified a rapid decrease in surface asperity within the first 10 min of the micro-Deval test, which corresponds to 5% cumulative abrasion. Paixão and Fortunato [19] found that the decrease in asperity of particles in a rotating drum was nearly the same during the first 2000 revolutions and the subsequent 12,000 revolutions. Fig. 5(b) shows how the probability distribution of r_a for the two particles varies with increasing A_l. Interestingly, the trend of the distribution change is similar for both particles, regardless of their initial shape. By comparing the histograms at different A_l levels, it becomes evident that concave asperities experience an even more rapid decrease and tend to disappear completely at higher A_l levels. This corresponds well to the experimental observations that particles subjected to high levels of abrasion tend to become nearly perfect convex shapes [27]. It is important to note that although the concave points are not directly abraded in our abrasion model, they are automatically decreased as the neighboring convex areas are eroded.

Fig. 6 presents the normalized histograms of r_a for all particles, comparing the initial and 30% abraded stages in a single graph. The mean values are represented by solid lines, while the maximum and minimum values are captured by the shaded areas. Notably, despite significant variations in the initial shapes, the local asperity distribution of all particles falls within a narrow range up to an abrasion level of 30%. This suggests that the evolution of asperity change can be considered a unique characteristic of ballast particles.

4. Simulation of triaxial compression tests using LS-DEM

4.1. LS-DEM

The level-set scheme-enriched discrete element method (LS-DEM), originally introduced in Kawamoto et al. [42], is employed in this study to simulate the behavior of railway ballast at different stages of abrasion. This method has been validated for accurately modeling arbitrarily shaped grain assemblies commonly encountered in geotechnics [43,44] and other engineering fields [45,46].

Within the LS-DEM framework, each particle is represented by its own level-set function (ϕ) and a bunch of discretized surface nodes. Contact detection is then performed through a node-to-surface algorithm widely used in finite element modeling, where the surface nodes ($\mathbf{p}_a^i$) of particle i (master) are compared against the level-set values (ϕ^j) of particle j (slave), as shown in Fig. 7. To ensure the accuracy of contact detection, a sufficiently high nodal density is required, as a low number of surface nodes may result in undetected initial contacts. In this study, an average of 2000 nodes are uniformly seeded onto the surface of each particle in the specimen. This density has been shown to provide adequate accuracy, as supported by previous research [36,42]. Further increasing the nodal density impacts only little on results while significantly increasing computational costs.

Since the LS-DEM formulation only affects contact detection, other components of the simulation, such as force computations and time integration, are not specific to LS-DEM and thus any implementation can be used such as those used in conventional DEM [47]. In this study, we adopt a linear spring-viscous damping force model and an explicit time integration scheme for simplicity.

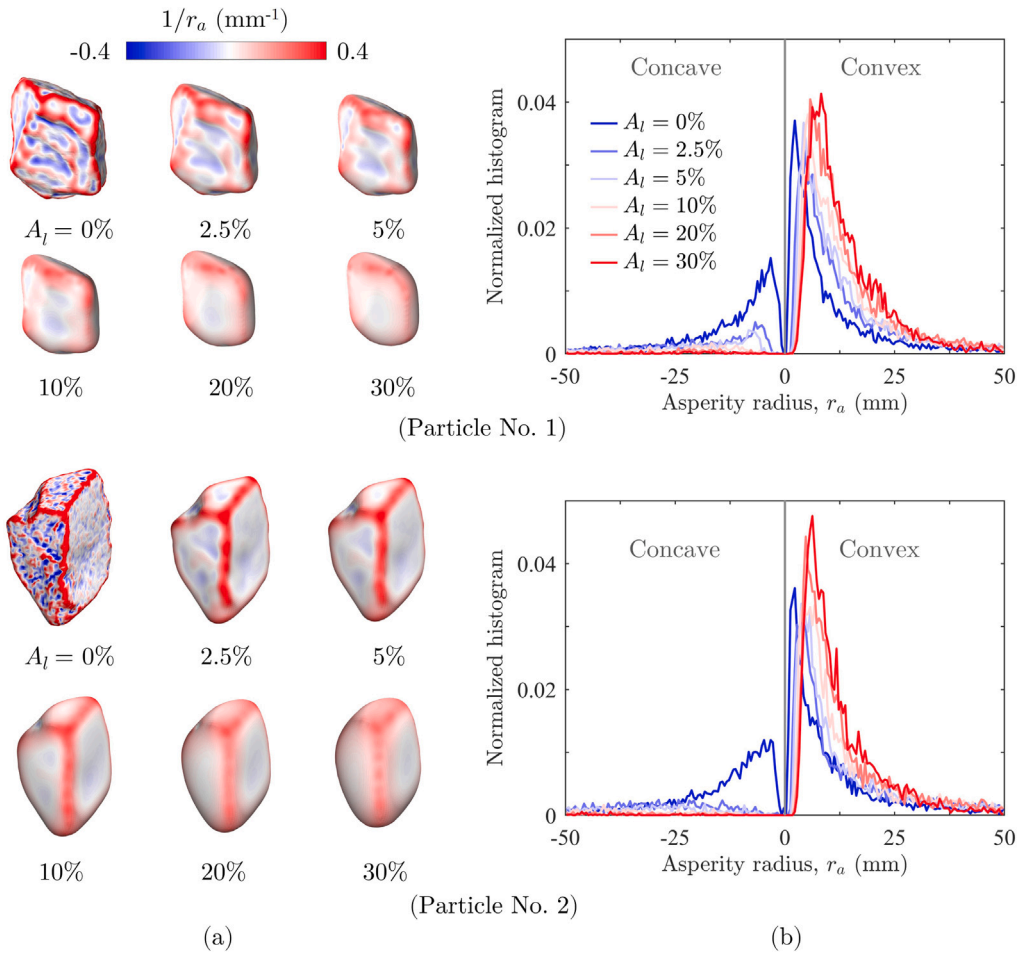

Fig. 5. (a) Visualizations and (b) normalized histograms of the asperity radii for two randomly selected particles at various abrasion levels. Negative values correspond to concave asperities and positive values to convex ones.

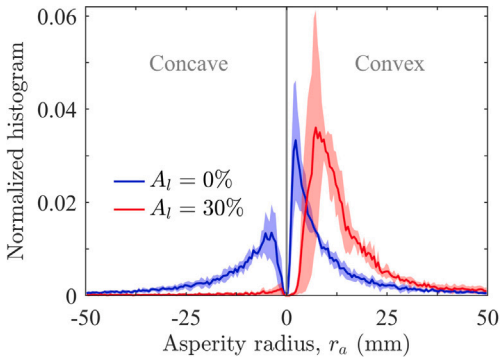

Fig. 6. Normalized histograms of the asperity radii for all particles at two abrasion levels: (a) $A_l = 0\%$; (b) $A_l = 30\%$. The solid line represent the average while the shaded areas represent the maximum and minimum values.

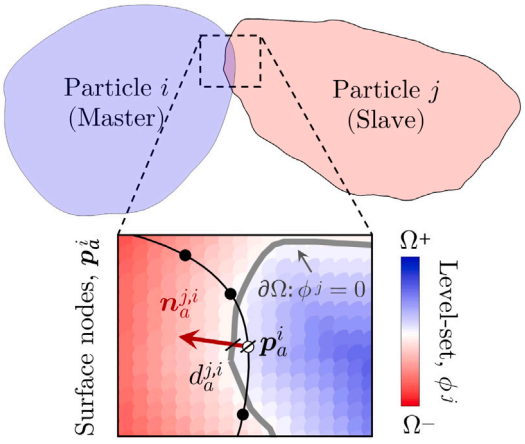

Fig. 7. 2D illustration of two contacting particles detected using the node-to-surface scheme in the LS-DEM framework.

4.2. Simulation description

Using the LS-DEM, we systematically perform high-fidelity simulations of drained true triaxial compression tests on both the fresh and computationally abraded railway ballast. For each level of abrasion, we first generate a ballast specimen consisting of n_p = 15,000 particles within a rigid cubical box using the 75 corresponding ballast shapes. In other words, each ballast shape is represented 200 times. The large number of particles, along with their representative size and shape distributions (as discussed in Section 2.1), helps ensure that the simulation results are both statistically meaningful and reproducible. The particles are assigned random orientations and positions to avoid initial overlaps and spatial correlations (i.e., inherent anisotropy). They are treated as rigid, ensuring that their size and shape remain unchanged throughout the simulations. Subsequently, the particles are slowly compressed from

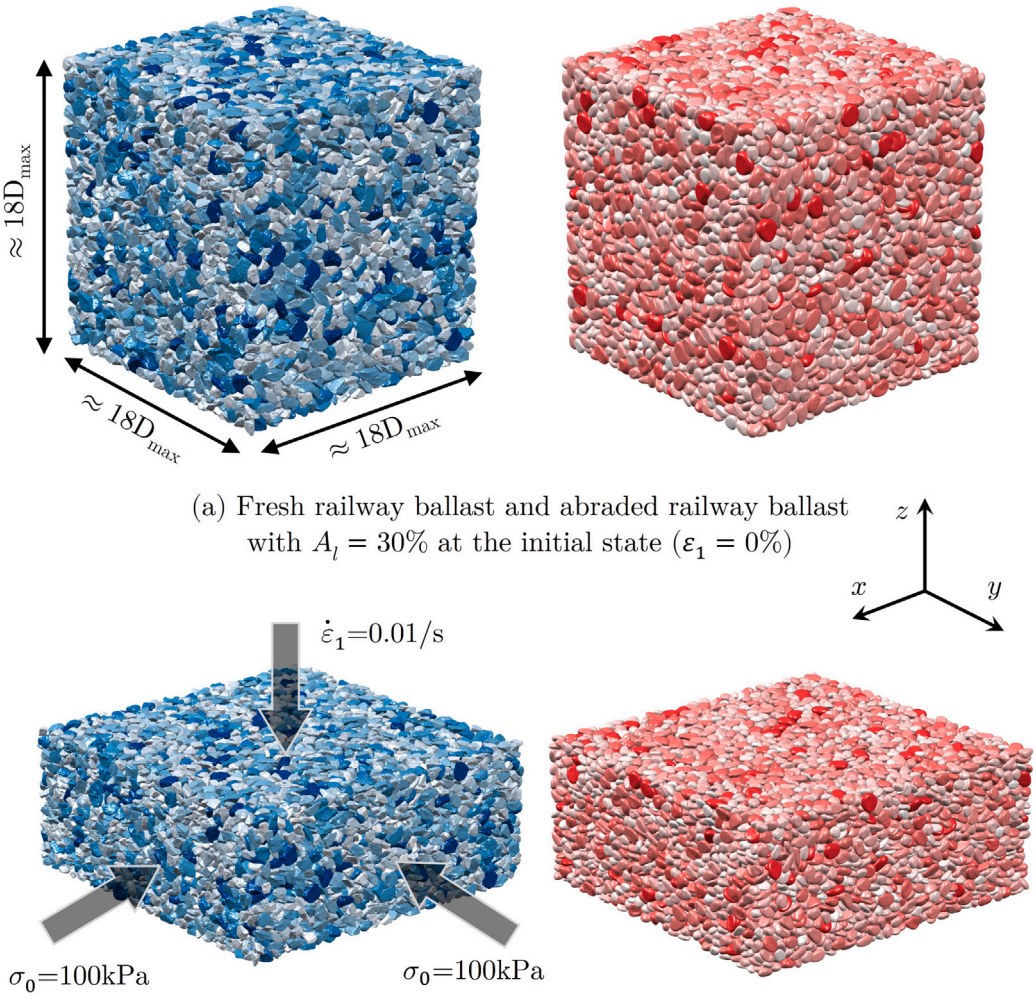

Fig. 8. Configurations of ballast specimens with $A_l = 0\%$ and $A_l = 30\%$ at (a) initial and (b) final states.

all directions by solid walls, following a standard isotropic compression protocol. During this phase, the friction coefficients between both the particles and walls, μ_{pw}, as well as between the particles themselves, μ_p, are set to zero. This strategy ensures the densest attainable packing within the virtual DEM environment, which is widely accepted by scholars to achieve a relative density (D_r) of 100% in the samples [48]. A constant confining pressure of $\sigma_0 = 100$ kPa is applied to the walls, and the stress within the ballast specimen is monitored throughout the compression. Note that the system stress is directly calculated from the internal forces across all particle contacts using the Love-Weber equation [49], rather than from the forces exerted on the solid walls. Specifically, the stress tensor is

$$\boldsymbol{\sigma} = \frac{1}{V}\sum_{\forall c} \boldsymbol{f}^c \otimes \boldsymbol{l}^c, \tag{7}$$

where $\boldsymbol{f}^c$ represents the contact force at contact c, $\boldsymbol{l}^c$ denotes the branch vector that connects the centroids of the particles involved in contact c, and V is the volume of the box enclosed by the walls. The isotropic compression continues until the system satisfies two conditions: (i) the system must reach mechanical equilibrium, determined by the kinetic energy (E_k) falling below a very small threshold $E_k < 10^{-10} k_n D_{50}^2$ per particle, where k_n is the constant spring stiffness in the normal direction. In our simulations, the values $k_n = k_s = 4 \times 10^6$ N/m are chosen to maintain particle rigidity (i.e., the average inter-particle penetration $\bar{\delta} < 10^{-3} D_{50}$) under external loading [50]; (ii) the system stresses, $\sigma_{xx} = \sigma_{yy} = \sigma_{zz}$, must reach the target confining pressure (σ_0). Fig. 8(a) illustrates the configurations of fresh and abraded ballast specimens prepared through isotropic compression. The void ratio of the compacted fresh ballast specimen is 0.583, which is nearly identical to the experimentally estimated minimum void ratio $e_{\min} = 0.596$ [50]. All virtual specimens have dimensions of at least $15D_{\max}$, which is sufficient to meet the requirements for the representative element volume (REV) [51].

Following sample preparation, the ballast specimens are subjected to quasi-static triaxial loading using a servo-controlled mechanism. During the shearing phase, a constant downward strain rate, $\dot{\varepsilon}_1 = 0.01\text{s}^{-1}$, is applied at the top boundary, while the lateral walls are adjusted accordingly to enforce a constant lateral confining pressure $\sigma_{xx} = \sigma_{yy} = 100$ kPa. The inter-particle friction coefficient (μ_p) is activated and set to 0.5, in accordance with values commonly observed in railway ballast [52,53]. Due to the rigid boundary conditions applied in the simulations, the specimens exhibit relatively smooth stress–strain and volume-strain behaviors at the macroscopic level. The stress ratio (q/p) is defined as the ratio of deviatoric stress (q) to mean stress (p), and the volumetric strain ($\varepsilon_v = \ln(V_0/V)$) is quantified through the volume change of the specimens. Additionally, the internal friction

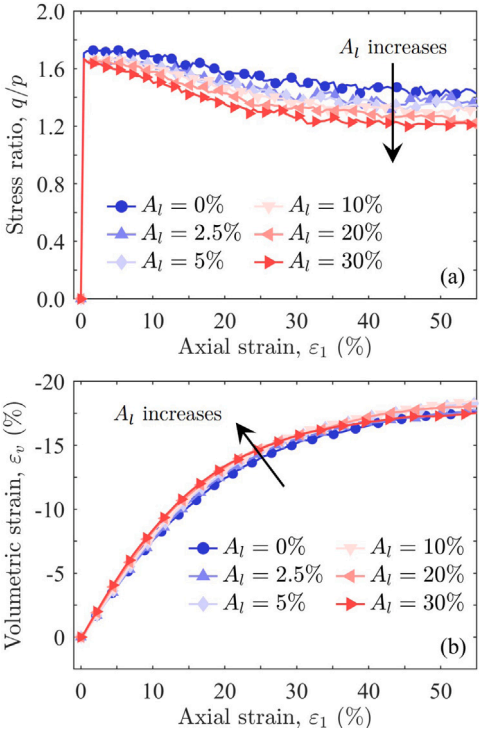

Fig. 9. Stress–strain and volumetric strain results from triaxial simulations of railway ballast under different abrasion levels: (a) q/p versus ε_1; (b) ε_v versus ε_1.

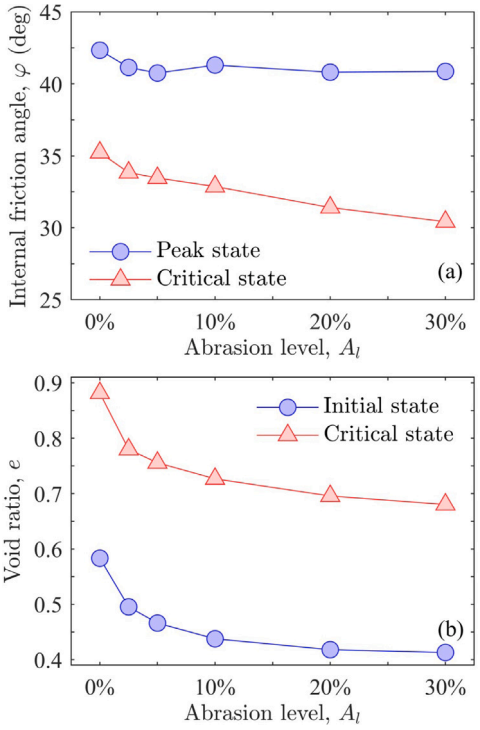

Fig. 10. Variations in (a) peak friction angle (φ_p) and critical friction angle (φ_c), and (b) initial void ratio (e_0) and critical void ratio (e_c), with abrasion level (A_l).

angle (φ) and void ratio (e) are used to characterize the macroscopic state of the deformed specimens. These parameters are tracked until they stabilize, indicating that the specimens have reached a critical state at large cumulative strains. In all simulations, the specimens are sheared to an axial strain (ε_1) of 55%, ensuring a clear identification of the critical state (Fig. 8(b)). In line with Zhao and Zhou [54] and our previous studies [48], the critical state is defined from $\varepsilon_1 = 40\%$ to the end of loading.

5. Mechanical response under triaxial compression

5.1. Stress–strain characteristics

Fig. 9 presents the evolution of q/p and ε_v as a function of ε_1. Qualitatively, specimens with higher A_l exhibit relatively lower stress levels throughout the loading process. After the strain-softening phase, the q/p values for different specimens decrease and stabilize, with the steady values stratified according to A_l. As expected, q/p decreases with increasing A_l, corresponding to the reduction in mechanical strength typically observed in the field due to abrasion. The peak and critical friction angles, denoted by φ_p and φ_c, are plotted against A_l in Fig. 10(a). Apart from fresh railway ballast, which shows a slightly higher φ_p, the peak stress states of specimens appear to be unaffected by A_l. Given that the peak strength of cohesionless granular materials is influenced by multiple factors instead shape irregularity alone, there must be a complex interplay among these factors. This will be discussed further in the following sections. In contrast, the critical state, which reflects the condition where all initial memory of the material is erased, is primarily governed by particle-scale properties. As we have isolated particle shape from all other properties, one can speculate on the nature of the difference in φ_c with reference only to shape. This explains why φ_c decreases monotonically with increasing A_l, as the abrasion continuously promotes the shape rounding of ballast particles.

The evolution of ε_v across the specimens does not show significant differences. This may be attributed to the fact that in dense granular

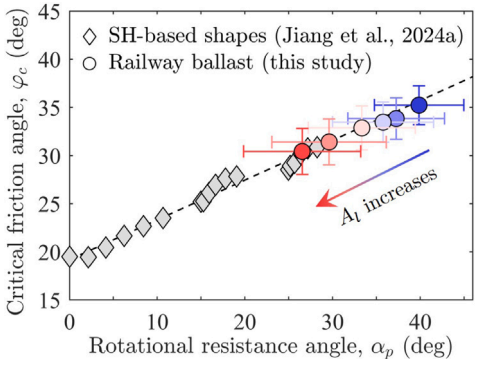

Fig. 11. Critical friction angle (φ_c) as a function of rotational resistance angle (α_p). The data for roughened ellipsoids from Jiang et al. [35] are shown as gray diamonds for comparison.

materials, the function $\varepsilon_v(\varepsilon_1)$ is primarily determined by the overall particle shape rather than finer shape details [35,55], while the overall form of studied ballast shapes changes little up to an abrasion level of 30% (see Section 3.2). This also explains why the peak strength of them is comparable, as φ_p is closely related to the additional dilation at the contacts between particles. The variations in initial and critical void ratios (e_0 and e_c) with A_l are illustrated in Fig. 10(b). Since the observed volumetric responses are similar, the compactness of the specimens relative to each other remains unchanged between the onset and the end of triaxial loading. Regarding the shape effect, within the explored abrasion range, both e_0 and e_c decrease sharply initially as the particles abrade, but then level off and gradually stabilize. This is likely because as A_l increases, particles are smoother and more ellipsoid-like, and it has been shown that ellipsoids pack at a higher volume fraction compared to angular blocks [56]. This finding is qualitatively consistent with the observation in fields that ballast degradation can cause settlement issues due to increased compactness. Furthermore,

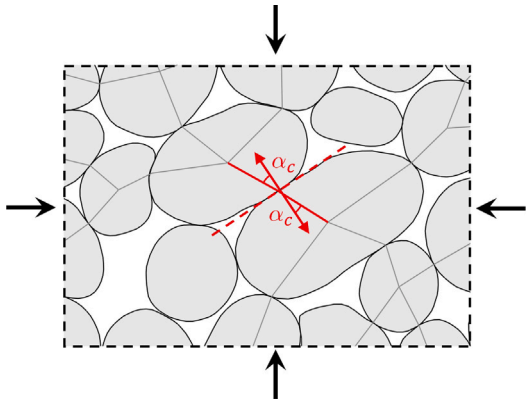

Fig. 12. Definition of the contact deviation angle (α_c). External work is required for deformation due to rolling resistance given by α_c.

the observed variation in φ_p with A_l can be potentially attributed to a balance between denser packing and decreased shape irregularity at higher abrasion levels.

Fig. 11 presents the relationship between the critical friction angle (φ_c) and the rotational resistance angle (α_p). The data indicates that the evolution of φ_c tracks fairly well with that of α_p; this further reinforces α_p as a robust, mechanically-based shape index. More notably, our results match perfectly with the data and linear fit reported by Jiang et al. [35], who identified that φ_c is linearly related to α_p for particles possessing multi-scale shape features. While Jiang et al. [35] investigated assemblies composed entirely of particles with a single shape artificially generated by spherical harmonics, our study examines assemblies of diverse ballast shapes to better replicate real-world conditions. Despite the variability in shape, which results in a wide distribution of α_p values among each ballast specimen, the average α_p remains valid in capturing this linear relationship. The standard deviations of α_p in each specimen is shown as error bars in Fig. 11. This finding further extends the applicability of α_p as a reliable shape index in more complex systems that encompass a diverse range of realistic particle shapes.

5.2. Contribution of contact subnetworks

The robust performance of the shape parameter (α_p) suggests that, inter-particle contacts with large contact deviation angles, denoted by α_c, between the contact normals and radial vectors (Fig. 12), are more common in specimens with lower A_l values and likely contribute more to the overall stability of the system. This is because such contacts are often associated with greater rotational hindrance from moments induced by normal contact forces. This observation forms the basis for contact subnetwork partitioning based on α_c, a strategy that has been widely adopted in the field of granular physics to evaluate the role of specific contact subnetworks in the stability of the granular skeleton [28,57,58].

Here, we divide the contacts into eight groups in terms of α_c values, with each group representing a 10-degree interval ranging from 0 to 80 degrees and forming contact subnetworks. Contacts with $\alpha_c > 80°$ have negligible weights and are therefore excluded from the analysis. The system stress tensor, $\boldsymbol{\sigma}$, can thus be split into stress contributions from each contact subnetwork:

$$\boldsymbol{\sigma} = \sum_{j=1}^{G} \boldsymbol{\sigma}^j, \tag{8a}$$

$$\boldsymbol{\sigma}^j = \frac{1}{V} \sum_{i=1}^{M_j} \boldsymbol{f}^i \otimes \boldsymbol{r}^i, \tag{8b}$$

where G represents the number of subnetworks and M_j denotes the number of contact branches within each subnetwork. It is important to note that $\boldsymbol{r}^i$ is the vector that connects the centroid to the contact point instead of centroid-to-centroid vector introduced in Eq. (7). Similarly, the deviatoric and mean stresses of each group, q^j and p^j, are respectively calculated from $\boldsymbol{\sigma}^j$:

$$q^j = \sigma_1^j - \sigma_3^j, \tag{9a}$$

$$p^j = \text{trace}(\boldsymbol{\sigma}^j)/3, \tag{9b}$$

where $q = \sum_{j=1}^{G} q^j$ and $p = \sum_{j=1}^{G} p^j$ are satisfied. By defining the stress ratio, q^j/p^j, for each contact subnetwork, we are allowed to assess their stability against external loading. The weight of each subnetwork j is denoted as $w^j = p^j/p$, and therefore, we can decompose the stress ratio into the contributions of each subnetwork as follows:

$$\frac{q}{p} = \sum_{j=1}^{G} \frac{q^j}{p^j} w^j. \tag{10}$$

Fig. 13 presents the evolution of q^j/p^j and w^j with respect to ε_1. For comparative purposes, we have selected two ballast specimens: one consisting of fresh ballast particles and the other composed of abraded ballast particles with $A_l = 20\%$. Initially, the q^j/p^j ratios for different partitioned subnetworks are all increased to relatively high values to indicate strain-hardening, even for contacts with low α_c angles. As loading progresses and dilation occurs, q^j/p^j for contacts whose α_c values are relatively lower decreases rapidly, mirroring the global stress-softening response shown in Fig. 9. In contrast, q^j/p^j for contacts with $\alpha_c > 50°$ remains almost unchanged even as the system gradually approaches the critical state. An intriguing and somewhat counter-intuitive observation is that, during the early stages of shearing, q^j/p^j for contacts with smaller α_c exhibits higher shear strength in ballast specimen with $A_l = 20\%$. We attribute this phenomenon to the ellipsoid-like shape of the abraded particles, which facilitates the formation of locally ordered clusters in the initially dense state. These shape-induced clusters can segregate particles into regions that share rotations and thus offer larger resistance in the early phases of shearing due to their structural stability [48]. Typically, the particles within these clusters tend to engage in contacts with relatively lower α_c values due to 'face'-to-'face' contacts. During the ongoing shearing, these cluster structures are gradually broken as the sample expands, leading to fragility (i.e., lower q^j/p^j) in the subnetworks characterized by lower α_c values. Conversely, at the critical state, the q^j/p^j ratios stratify according to contact groups, with contacts having larger α_c generally possessing stronger stability (or exhibiting higher q^j/p^j) under external loading than those with lower α_c. As a result, specimens with less abraded particles can sustain higher macroscopic q/p ratios in the residual state compared to specimens where particle shapes experience more significant abrasion.

Regarding the variation of w^j with ε_1, the results indicate that shearing has only little impact on these weights, which are primarily dependent on A_l and remain unchanged throughout the loading. For abraded railway ballast with $A_l = 20\%$, it is rare to find contacts with $\alpha_c > 60°$, as surface wear reduces the presence of sharp edges and angular corners. Nevertheless, in both fresh and abraded ballast, contacts with α_c below 50 degrees are dominant, leading to the strain-softening behavior observed in the global q/p curves.

The detailed variations in $(q^j/p^j)_c$ and w_c^j at the critical state as functions of α_p are summarized in Fig. 14. For any given α_p, $(q^j/p^j)_c$ decreases with increasing α_c, with its value nearly reduced by half when comparing contacts with $\alpha_c \in [70, 80]°$ to those with $\alpha_c \in [0, 10]°$. This suggests that contact subnetworks formed by larger contact deviation angles are generally associated with greater mechanical stability. This is because the resisting moment induced by normal forces scales with increasing α_c, and it is expected that contacts with higher α_c provide stronger interlocking effects. Regarding the influence of particle abrasion, its primary effect appears to be on the proportions of

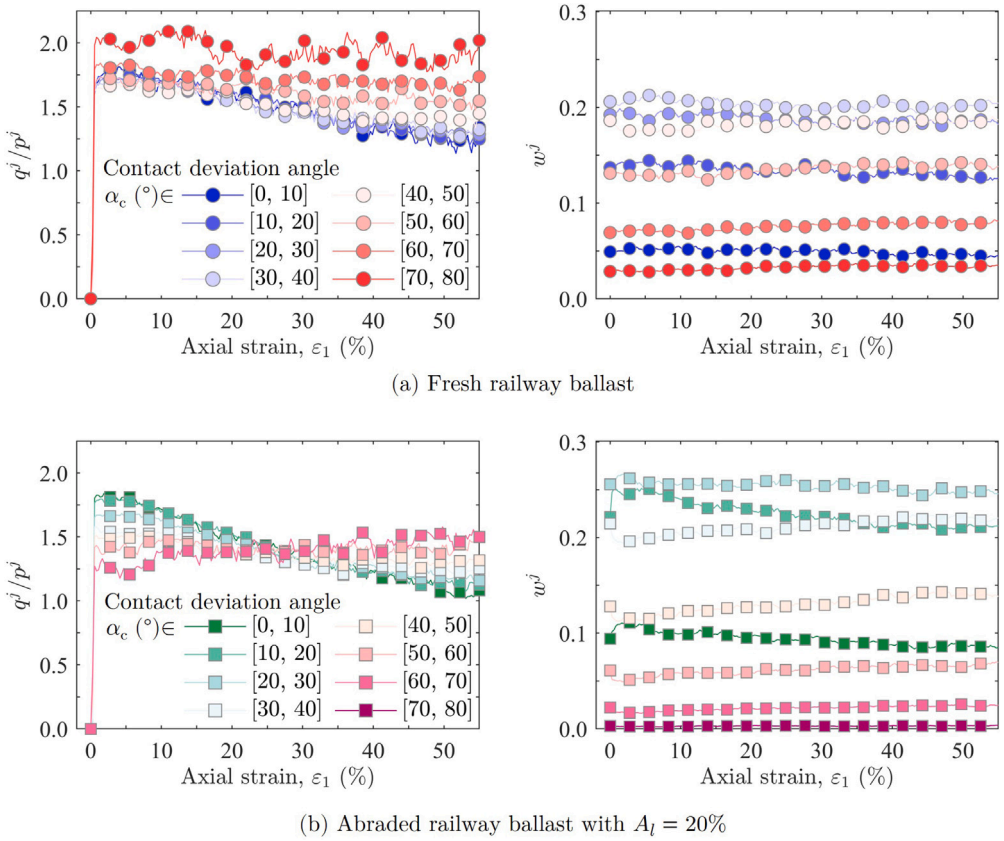

Fig. 13. Variations in stress ratio (q^j/p^j) and corresponding weight (w^j) of contact subnetworks in specimens of (a) fresh railway ballast and (b) abraded railway ballast with $A_l = 20\%$, as a function of axial strain (ε_1). Contacts with $\alpha_c > 80°$ have negligible weights and are neglected.

different contact groups (w_c^j). Specifically, as abrasion progresses, w_c^j of contacts with $\alpha_c \geq 40°$ (i.e., more stable contacts) decreases, while those with $\alpha_c \leq 30°$ (i.e., less stable contacts) increase monotonically. Furthermore, the fraction of contacts with $\alpha_c \in [30, 40]°$ remains largely unchanged. Consequently, due to the combined effect of a changed w^j distribution and a slightly weakened $(q^j/p^j)_c$ with increasing A_l (or decreasing α_p), the overall system strength has a continuous decline.

5.3. Friction mobilization

Lower shape irregularity due to particle abrasion tends to more promote the rotational motion of particles, and as a result, the slip motion is restricted and the friction at contacts is less mobilized. In order to capture this feature, we then define and explore the friction mobilization, $I_m = \overline{f_t/f_n}$, where f_t and f_n denote the magnitudes of tangential and normal forces at the same contacts. Fig. 15(a) shows the evolution of I_m with ε_1 for all specimens. We observe that I_m has a similar behavior to macroscopic stresses that it has a rapid enhancement at the beginning followed by the decline and stabilization at the critical state. Within the simulated strain range, I_m curves stratify according to A_l, with a larger A_l typically leading to lower I_m. This anticipated dependence indicates that abraded particles have lower hindrance to rotations and particles can escape from contacts easily before the tangential force reaches the sliding threshold decided by the friction coefficient.

By further plotting critical-state friction mobilization ($I_{m,c}$) as a function of α_p (Fig. 15(b)), we observe that the data for ballast specimens match well with the trend previously reported for roughened ellipsoids [35], where $I_{m,c}$ increases monotonically from 0.29 for weakly interlocked spheres ($\alpha_p = 0$) to 0.42 for fresh railway ballast. This finding highlights that α_p is a surprisingly robust parameter for quantifying particle shape effects in a granular system even from a microscopic perspective. For fresh railway ballast, $I_{m,c}$ closely approaches the upper limit dictated by $\mu_p = 0.5$, suggesting that intact ballast particles possess a high degree of surface roughness and angularity to effectively resist the rotation and mobilize the friction. After experiencing up to 30% mass loss due to abrasion, the particles remain sufficiently irregular, allowing the specimen to retain nearly 90% of its intact-state friction mobilization capacity. In addition to its direct contribution to macroscopic shear strength [59,60], we expect that variation in $I_{m,c}$ partially accounts for the differences in void ratio observed in Fig. 10(b). Specifically, higher values of $I_{m,c}$ promote the formation of stable internal structures and contact networks, enabling the existence of larger voids within the specimen.

5.4. Shear-induced anisotropy

Fig. 16 illustrates snapshots of normalized force chains ($f_n/\bar{f}_n$) for two selected specimens at the critical state, where $\bar{f}_n$ denotes the sample-averaged normal force. These force chains are depicted as segments connecting particle centroids to the surrounding contact points, with their magnitudes represented by the thickness and color intensity of the segments. A visual inspection on the force chains and contact normal distributions reveals the anisotropic and inhomogeneous nature of the contact network, marked by the formation of more pronounced and stronger force chains concentrated along the vertical direction (or maximum principal stress direction). It is well established that the presence of anisotropy in a granular system is inherently linked to its macroscopic stress behavior, which in turn, helps explain how various anisotropic components contribute to bulk strength and their sensitivity to particle-scale properties. However, these characteristics cannot be quantitatively assessed solely through visual interpretation of Fig. 16.

For a more quantitative assessment, previous studies have established an explicit stress-force-fabric relationship to directly correlate

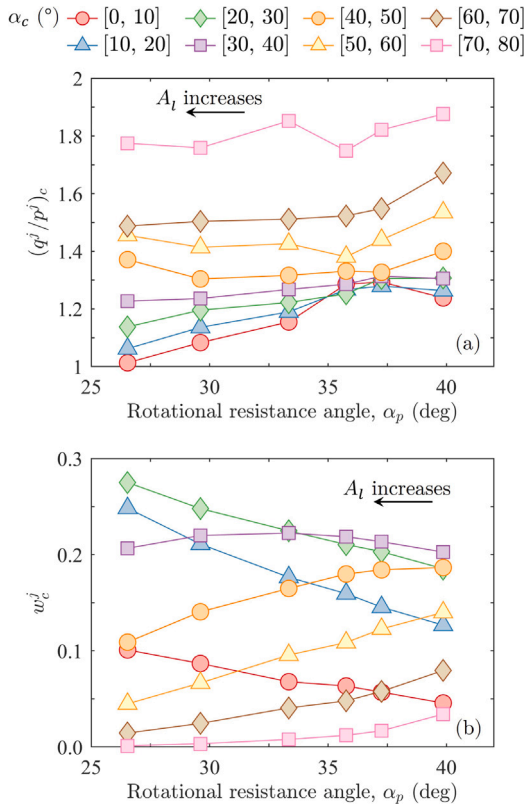

Fig. 14. (a) Stress ratio ($(q^j/p^j)_c$) at the critical state of groups of contacts with varying ranges of α_c. (b) Weights (w_c^j) of these groups at the critical state. Contacts with $\alpha_c > 80°$ have negligible weights and are neglected.

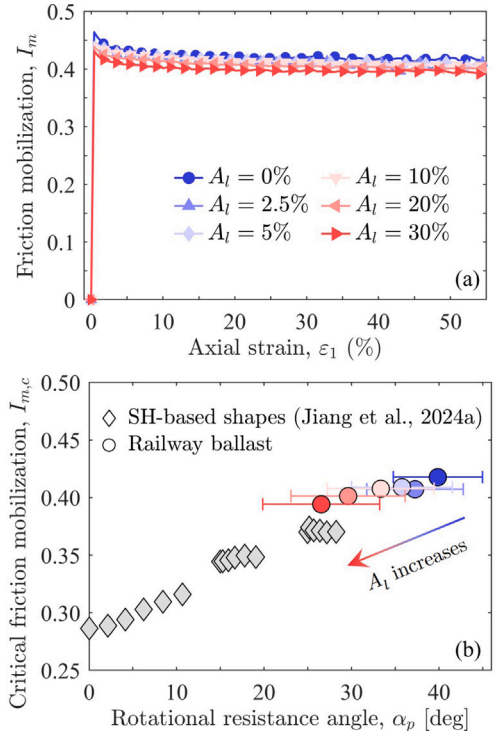

Fig. 15. (a) Evolution of friction mobilization ($I_m = \overline{f_t/f_n}$) with axial strain (ε_1) for ballast specimens with different abrasion levels (A_l). (b) Critical friction mobilization ($I_{m,c}$) as a function of rotational resistance angle (α_p). The data for roughened ellipsoids from Jiang et al. [35] are shown as gray diamonds for comparison.

the system stress ratio (q/p) with shear-induced anisotropy across both geometrical and mechanical aspects (a_*):

$$\frac{q}{p} \simeq a_c + a_n + a_t + a_{cf} + a_s, \tag{11}$$

where a_c, a_n, and a_t are the anisotropies of contact normals, normal forces, and tangential forces, respectively. The terms a_{cf} and a_s describe the anisotropy associated with the correlation between contact normals and normal forces, and the anisotropy arising from the effect of particle shape, respectively. For a full derivation of Eq. (11) and the computation of corresponding scalar anisotropy coefficients, readers are referred to Zhao et al. [61].

Fig. 17(a) compares the critical stress ratio, $(q/p)_c$, calculated from the stress tensor using Eq. (7), with its approximation based on the microscopic anisotropy components in Eq. (11). The results indicate that all data points lie near the line $(q/p)_c = a_{c,c} + a_{n,c} + a_{t,c} + a_{cf,c} + a_{s,c}$, confirming the applicability of Eq. (11) in granular systems with variously shaped ballast particles. Fig. 17(b) further evaluates the contribution of each anisotropy component to the critical stress ratio and their shape-dependence by plotting $a_{*,c}$ against α_p. Similar to the findings of Zhao et al. [61] and Jiang et al. [35], $a_{c,c}$ and $a_{n,c}$ play the primary roles within the positive contributors (i.e., $a_{c,c}$, $a_{n,c}$, $a_{t,c}$, and $a_{cf,c}$), whereas $a_{s,c}$ exerts a negative influence.

Regarding the effects of particle abrasion, all positive contributors decrease with decreasing α_p, while $a_{s,c}$ exhibits an increase. However, the rise in $a_{s,c}$ is insufficient to offset the reductions in the other components, leading to a monotonic decline in $(q/p)_c$. Notably, $a_{c,c}$ has the most significant reduction with increasing A_l, making it the primary factor resulting in the abrasion-induced reduction in strength. This observation agrees well with the findings of Jiang et al. [35] and is supported by the discussions on partitioned contact network in Section 5.2, where a higher A_l correlates with reduced tortuosity of contact paths.

6. Conclusions and future directions

In this study, we present a computational abrasion model to predict the abraded shapes of railway ballast particles by applying a relationship between Gaussian curvature and abrasion depth based on Firey's law. Using this model, we simulate the abrasion of 75 particles from fresh railway ballast scans to predict their shape evolution at various stages of abrasion. Additionally, we perform LS-DEM simulations of triaxial compression tests to investigate the evolution of shear strength and void ratio with abrasion extent under identical shear conditions. The major findings are summarized as follows:

- The level-set function is essential to the proposed abrasion framework, as it enables an accurate representation of particle shape and the computation of various properties, including their inertial properties and surface curvature. Furthermore, by modifying the level-set function, we can simulate the process of particle abrasion. When integrated with the DEM method, it allows for the discrete modeling of railway ballast with complex shapes resulting from different abrasion levels.
- The evolution of particle shapes predicted by the computational abrasion model agrees well with experimental observations in the literature, showing its efficiency and potential for broader applications. The findings indicate that, up to an abrasion level of 30%, the overall particle form of a ballast particle remains largely sustained, while primary changes occur in its local angularity and surface asperity. The surface asperity decreases rapidly in the early stages of abrasion, causing the particles to smooth out quickly. In contrast, the loss of angularity is more gradual and continuous.
- The triaxial compression tests show that macroscopically both the stress ratio and void ratio decrease with increasing abrasion

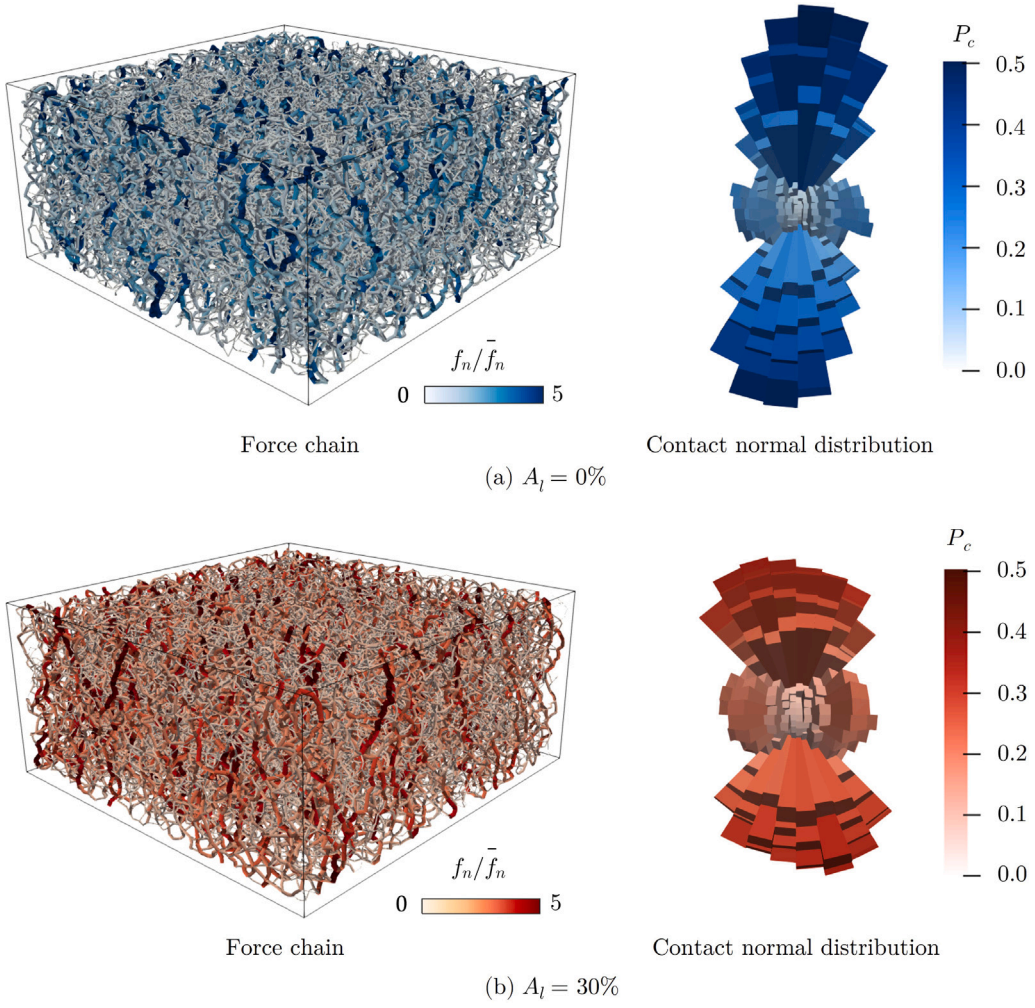

Fig. 16. Snapshots of force chains (left) and contact normal distributions (right) in the specimens at the critical state for (a) $A_l = 0\%$ and (b) $A_l = 30\%$. Line thickness and color intensity in the force chains are proportional to the normalized normal force magnitude ($f_n/\bar{f}_n$).

levels. By decomposing the stress ratio into the contributions from contact subnetworks or microscopic anisotropy components, we show that the decrease in stress ratio can be attributed to the decrease of stable contacts with larger contact deviation angles or to reduction in contact network anisotropy. In contrast, the decrease in void ratio is mainly attributed to the transition of particles toward ellipsoid-like shapes, which are less interlocked and easier to reorient, leading to stronger ordered alignment and more compact packing. Additionally, the rotational resistance angle is identified as a robust shape parameter that captures the behavioral changes induced by shape change occurring at multiscales. It has the potential to be applied in real-world ballast fouling assessments as a supplement to other geometry-based shape descriptors.

While the proposed model is based on level-set functions, it can also be applied to other DEM codes that use more widely adopted shape representation schemes, such as clumps or polyhedra. In such cases, the particle surface mesh must be explicitly extracted from the level-set grid by identifying the zeroth isosurface, after which clumps or polyhedra can be constructed accordingly. However, faithfully capturing abrasion-induced shape changes may require a large number of sub-spheres (in clumps) or faces (in polyhedra), which can significantly increase computational cost.

Future work with the proposed model will certainly include quantitative validation through well-controlled experiments that track the shape evolution of individual ballast particles. Further work may also involve integration with the breakage model proposed by Harmon et al. [62], which takes the advantage of level-set functions to simulate particle splitting. Such a combined framework could support more realistic modeling of ballast degradation for practical applications.

CRediT authorship contribution statement

Haoran Jiang: Writing – original draft, Visualization, Validation, Software, Methodology, Investigation, Funding acquisition, Data curation. **Opu Chandra Debanath:** Writing – review & editing, Visualization, Software, Methodology, Investigation, Data curation, Conceptualization. **Yang Li:** Writing – review & editing, Investigation, Data curation. **Ruidong Li:** Writing – review & editing, Software, Investigation, Data curation.

Declaration of competing interest

The authors declare that they have no known competing financial interests or personal relationships that could have appeared to influence the work reported in this paper.

Acknowledgments

This work was supported by JST-SPRING program Grant Number JPMJSP2124.

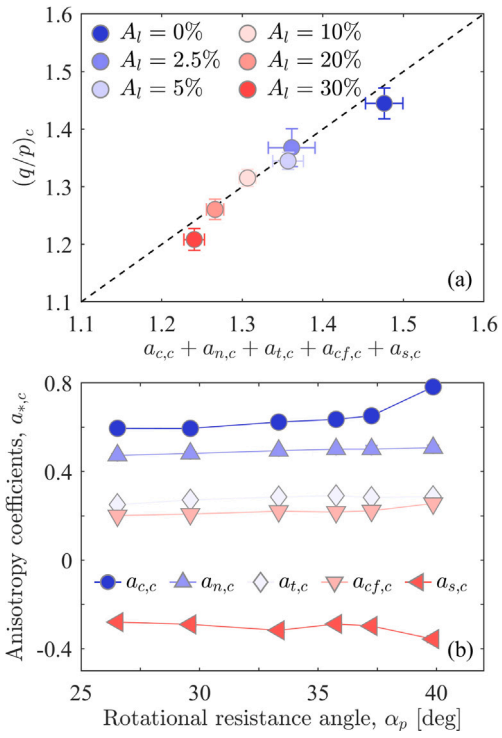

Fig. 17. (a) Comparison of $(q/p)_c$ computed from Eq. (7) with its approximation computed from Eq. (11). (b) Anisotropy coefficients ($a_{*,c}$) at the critical state as a function of rotational resistance angle (α_p).

Appendix. Physical properties of ballast particles computed from level-set function

For the purposes of building new particles from abrasion, we present the way to determine their inertial properties using solely the level-set function (ϕ). The smoothed Heaviside function, $H(\phi)$, is introduced as a weighting function, defined as:

$$H(\phi) = \begin{cases} 0 & \text{if } \phi \le -\epsilon, \\ [1 + \phi/\epsilon + \sin(\pi\phi/\epsilon)/\pi]/2 & \text{if } -\epsilon < \phi \le \epsilon, \\ 1 & \text{if } \phi > \epsilon. \end{cases} \tag{A.1}$$

Here, the smoothness parameter $\epsilon = 1.5$ is chosen [42]. Under the assumption that the density is uniformly distributed within a ballast particle, the particle's mass is given by:

$$m = \rho g^3 \sum_{i=1}^{I}\sum_{j=1}^{J}\sum_{k=1}^{K} H(-\phi(x_i, y_j, z_k)), \tag{A.2}$$

where ρ is the particle density, g is the grid spacing, and I, J, and K denote the number of grid points in the x-, y-, and z-directions of ϕ, respectively. The center of mass is calculated as:

$$c_x = \frac{\rho g^3}{m} \sum_{i=1}^{I}\sum_{j=1}^{J}\sum_{k=1}^{K} H(-\phi(x_i, y_j, z_k))x_i, \tag{A.3a}$$

$$c_y = \frac{\rho g^3}{m} \sum_{i=1}^{I}\sum_{j=1}^{J}\sum_{k=1}^{K} H(-\phi(x_i, y_j, z_k))y_j, \tag{A.3b}$$

$$c_z = \frac{\rho g^3}{m} \sum_{i=1}^{I}\sum_{j=1}^{J}\sum_{k=1}^{K} H(-\phi(x_i, y_j, z_k))z_k. \tag{A.3c}$$

Finally, the moment of inertial is:

$$I_{11} = \rho g^3 \sum_{i=1}^{I}\sum_{j=1}^{J}\sum_{k=1}^{K} H(-\phi(x_i, y_j, z_k))[(y_j - c_y)^2 + (z_k - c_z)^2], \tag{A.4a}$$

$$I_{22} = \rho g^3 \sum_{i=1}^{I}\sum_{j=1}^{J}\sum_{k=1}^{K} H(-\phi(x_i, y_j, z_k))[(x_i - c_x)^2 + (z_k - c_z)^2], \tag{A.4b}$$

$$I_{33} = \rho g^3 \sum_{i=1}^{I}\sum_{j=1}^{J}\sum_{k=1}^{K} H(-\phi(x_i, y_j, z_k))[(x_i - c_x)^2 + (y_j - c_y)^2], \tag{A.4c}$$

$$I_{23} = I_{32} = -\rho g^3 \sum_{i=1}^{I}\sum_{j=1}^{J}\sum_{k=1}^{K} H(-\phi(x_i, y_j, z_k))(y_j - c_y)(z_k - c_z), \tag{A.4d}$$

$$I_{13} = I_{31} = -\rho g^3 \sum_{i=1}^{I}\sum_{j=1}^{J}\sum_{k=1}^{K} H(-\phi(x_i, y_j, z_k))(x_i - c_x)(z_k - c_z), \tag{A.4e}$$

$$I_{12} = I_{21} = -\rho g^3 \sum_{i=1}^{I}\sum_{j=1}^{J}\sum_{k=1}^{K} H(-\phi(x_i, y_j, z_k))(x_i - c_x)(y_j - c_y). \tag{A.4f}$$

Data availability

Data will be made available on request.

References

[1] Lu M, McDowell G. Discrete element modelling of ballast abrasion. Géotechnique 2006;56(9):651–5.
[2] Lobo-Guerrero S, Vallejo LE. Discrete element method analysis of railtrack ballast degradation during cyclic loading. Granul Matter 2006;8:195–204.
[3] Qian Y, Boler H, Moaveni M, Tutumluer E, Hashash YM, Ghaboussi J. Characterizing ballast degradation through los angeles abrasion test and image analysis. Transp Res Rec 2014;2448(1):142–51.
[4] Guo Y, Markine V, Qiang W, Zhang H, Jing G. Effects of crumb rubber size and percentage on degradation reduction of railway ballast. Constr Build Mater 2019;212:210–24.
[5] Rohrman AK, Kashani HF, Ho CL. Effects of natural abrasion on railroad ballast strength and deformation properties. Constr Build Mater 2020;247:118315.
[6] Hu Q, Gao R, Chen J, Yuan Z. Experimental study and theoretical analysis on ballast particle crushing based on energy dissipation and release. Powder Technol 2024;439:119664.
[7] Kumara JJ, Hayano K. Deformation characteristics of fresh and fouled ballasts subjected to tamping maintenance. Soils Found 2016;56(4):652–63.
[8] Xu C, Ito K, Hayano K, Momoya Y. Combined effect of supported and unsupported sleepers on lateral ballast resistance in ballasted railway track. Transp Geotech 2023;38:100913.
[9] Indraratna B, Nimbalkar SS, Tennakoon N. The behaviour of ballasted track foundations: track drainage and geosynthetic reinforcement. In: GeoFlorida 2010: advances in analysis, modeling & design. 2010, p. 2378–87.
[10] Mahmoud E, Papagiannakis A, Renteria D. Discrete element analysis of railway ballast under cycling loading. Procedia Eng 2016;143:1068–76.
[11] Wentworth CK. A laboratory and field study of cobble abrasion. J Geol 1919;27(7):507–21.
[12] Kodama Y. Experimental study of abrasion and its role in producing downstream fining in gravel-bed rivers. J Sediment Res 1994;64(1a):76–85.
[13] Lewin J, Brewer P. Laboratory simulation of clast abrasion. Earth Surf Process Landforms: J Br Geomorphol Res Group 2002;27(2):145–64.
[14] Firey WJ. Shapes of worn stones. Mathematika 1974;21(1):1–11.
[15] Domokos G, Sipos AÁ, Várkonyi PL. Countinuous and discrete models for abrasion processes. Period Polytech Archit 2009;40(1):3–8.
[16] Domokos G, Jerolmack DJ, Sipos AÁ, Török Á. How river rocks round: resolving the shape-size paradox. PLoS One 2014;9(2):e88657.
[17] Deiros Quintanilla I, Combe G, Emeriault F, Voivret C, Ferellec JF. X-ray CT analysis of the evolution of ballast grain morphology along a Micro-Deval test: key role of the asperity scale. Granul Matter 2019;21(2):30.
[18] Ge H, Sha A, Han Z, Xiong X. Three-dimensional characterization of morphology and abrasion decay laws for coarse aggregates. Constr Build Mater 2018;188:58–67.
[19] Paixão A, Fortunato E. Abrasion evolution of steel furnace slag aggregate for railway ballast: 3D morphology analysis of scanned particles by close-range photogrammetry. Constr Build Mater 2021;267:121225.
[20] Bloore F. The shape of pebbles. J Int Assoc Math Geol 1977;9:113–22.
[21] Finnie I. Erosion of surfaces by solid particles. Wear 1960;3(2):87–103.
[22] Archard JF, Hirst W. The wear of metals under unlubricated conditions. Proc R Soc A 1956;236:397–410.
[23] Deiros Quintanilla I, Combe G, Emeriault F, Toni JB, Voivret C, Ferellec JF. Wear of sharp aggregates in a rotating drum. In: EPJ web of conferences, vol. 140, EDP Sciences; 2017, p. 07009.
[24] De Bono J, Li H, McDowell G. A new abrasive wear model for railway ballast. Soils Found 2020;60(3):714–21.

[25] Gong J, Huang D, Mei G, Jiang J, Jiang M, Ou X, Chen M. New crushing criterion invariant to the coordination number effect in discrete element modelling. Acta Geotech 2024;19(5):3257–72.
[26] Zhang ZT, Gao WH, Wang X, Zhang JQ, Tang XY. Degradation-induced evolution of particle roundness and its effect on the shear behaviour of railway ballast. Transp Geotech 2020;24:100388.
[27] Binaree T, Kwunjai S, Jitsangiam P, Azéma E, Jing G. Assessment of macro and micro mechanical properties of fresh and deteriorated ballast combining laboratory tests and 2D-discrete element methods. Constr Build Mater 2024;420:135525.
[28] Tolomeo M, McDowell GR. Modelling real particle shape in DEM: a comparison of two methods with application to railway ballast. Int J Rock Mech Min Sci 2022;159:105221.
[29] Kawamoto R, Andò E, Viggiani G, Andrade JE. All you need is shape: Predicting shear banding in sand with LS-DEM. J Mech Phys Solids 2018;111:375–92.
[30] Osher S, Fedkiw R, Piechor K. Level set methods and dynamic implicit surfaces. Appl Mech Rev 2004;57(3). B15–B15.
[31] Li R, Hu X, Chen F, Wang X, Xiong H, Wu H. A systematic framework for DEM study of realistic gravel-sand mixture from particle recognition to macro-and micro-mechanical analysis. Transp Geotech 2022;34:100693.
[32] Paixão A, Resende R, Fortunato E. Photogrammetry for digital reconstruction of railway ballast particles–A cost-efficient method. Constr Build Mater 2018;191:963–76.
[33] Kumara JJ, Hayano K, Kikuchi Y. Evaluation of area-and volume-based gradations of sand-crushed stone mixture by 2D images. Ksce J Civ Eng 2017;21:774–81.
[34] Kawamoto R, Andrade J, Matsushima T. A 3-D mechanics-based particle shape index for granular materials. Mech Res Commun 2018;92:67–73.
[35] Jiang H, Debanath OC, Chen F, Kawamoto R, Li Y. Analyzing the mechanical behavior of granular materials: A multi-morphological approach using spherical harmonics and LS-DEM. Powder Technol 2024;445:120078.
[36] Duriez J, Bonelli S. Precision and computational costs of level set-discrete element method (LS-DEM) with respect to DEM. Comput Geotech 2021;134:104033.
[37] Várkonyi P, Domokos G. A general model for collision-based abrasion processes. IMA J Appl Math 2011;76(1):47–56.
[38] Montero-Cubillo N, Estaire J, Marull E. Ballast degradation under different cycles and rotational speeds in micro-Deval equipment. In: Geotechnical engineering challenges to meet current and emerging needs of society. CRC Press; 2024, p. 3159–64.
[39] Bruzek R, Stark TD, Wilk ST, Thompson HB, Sussmann Jr TR. Fouled ballast definitions and parameters. In: ASME/iEEE joint rail conference, vol. 49675, American Society of Mechanical Engineers; 2016, V001T01A007.
[40] Alessandro M, Paolo C. PyMeshLab. Zenodo; 2021.
[41] Guennebaud G, Gross M. Algebraic point set surfaces. In: ACM siggraph 2007 papers. 2007, pp. 23–es.
[42] Kawamoto R, Andò E, Viggiani G, Andrade JE. Level set discrete element method for three-dimensional computations with triaxial case study. J Mech Phys Solids 2016;91:1–13.
[43] Perozzi D, Andrade J, Kaufmann R, Puzrin AM. LS-DEM guided analysis of geotechnical tests: Exploring strength anisotropy and stress dependency. J Geotech Geoenvironmental Eng 2025;151(3):04025001.
[44] Cui J, Karapiperis K, Torgersrud Ø, Andò E, Viggiani G, Andrade J. Deciphering necking in granular materials: Micromechanical insights into sand behavior during cycles of triaxial compression and extension. J Mech Phys Solids 2025;106022.
[45] Moncada R, Gupta M, Thompson A, Andrade JE. Level set discrete element method for modeling sea ice floes. Comput Methods Appl Mech Engrg 2023;406:115891.
[46] Harmon JM, Gabuchian V, Rosakis AJ, Conte JP, Restrepo JI, Rodriguez A, Nema A, Pedretti AR, Andrade JE. Predicting the seismic behavior of multiblock tower structures using the level set discrete element method. Earthq Eng Struct Dyn 2023;52(9):2577–96.
[47] Cundall P, Strack O. A discrete numerical model for granular assemblies. Geotechnique 1979;29(1):47–65.
[48] Jiang H, Kawamoto R, Li Y. Shape-induced clusters of ellipsoids during triaxial compression: A multiscale analysis using LS-DEM. Comput Geotech 2024;169:106235.
[49] Cantor D, Azéma E, Preechawuttipong I. Microstructural analysis of sheared polydisperse polyhedral grains. Phys Rev E 2020;101(6):062901.
[50] Tolomeo M, McDowell GR. DEM study of an "avatar" railway ballast with real particle shape, fabric and contact mechanics. Granul Matter 2023;25(2):32.
[51] Cantor D, Ovalle C. Sample size effects on the critical state shear strength of granular materials with varied gradation and the role of column-like local structures. Géotechnique 2023;1–12.
[52] Guo Y, Zhao C, Markine V, Jing G, Zhai W. Calibration for discrete element modelling of railway ballast: A review. Transp Geotech 2020;23:100341.
[53] Jiang H, Debanath OC, Kawamoto R, Matsushima T, Adachi S, Miwa M. Calibration of railway ballast modeling using level set discrete element method. In: International conference on computational & experimental engineering and sciences. Springer; 2023, p. 1–15.
[54] Zhao S, Zhou X. Effects of particle asphericity on the macro-and micro-mechanical behaviors of granular assemblies. Granul Matter 2017;19:1–18.
[55] Li Y, Otsubo M, Angelidakis V, Kuwano R, Nadimi S. Exploring the micro-to-macro response of granular soils with real particle shapes by way of μCT-aided DEM analyses. Géotechnique 2024;1–14.
[56] Li Y, Otsubo M, Liu J, Kuwano R. Effect of particle morphology on stress and strain characteristics of granular materials during triaxial compression. Acta Geotech 2024;19(5):2753–73.
[57] Azéma E, Radjai F. Force chains and contact network topology in sheared packings of elongated particles. Phys Rev E (3) 2012;85(3):031303.
[58] Li Y, Jiang H. Investigating rotational characteristics and contact mechanisms of star-like shapes using multiellipse-based DEM. Particuology 2025;99:210–25.
[59] Nie J, Zhao S, Cui Y, Wang Y. Coupled effects of particle overall regularity and sliding friction on the shear behavior of uniformly graded dense sands. J Rock Mech Geotech Eng 2022;14(3):873–85.
[60] Krengel D, Jiang H, Chen J, Matsushima T. The combined effect of particle angularity and inter-particle friction on micro-and macroscopic properties of granular assemblies. Comput Geotech 2025;177:106850.
[61] Zhao S, Evans TM, Zhou X. Shear-induced anisotropy of granular materials with rolling resistance and particle shape effects. Int J Solids Struct 2018;150:268–81.
[62] Harmon JM, Arthur D, Andrade JE. Level set splitting in DEM for modeling breakage mechanics. Comput Methods Appl Mech Engrg 2020;365:112961.